

1
2
3
4
5
6
7
8
9
10
11
12
13
14
15
16
17
18
19
20
21
22
23
24
25
26
27
28
29
30
31
32
33
34
35
36
37
38
39
40
41
42
43
44
45

Development of low-cost multi-wavelength imager system for studies of auroras and airglows

Ogawa, Y.^{1,2,3}, Y. Tanaka^{1,2,3}, A. Kadokura^{1,2,3}, K. Hosokawa⁴, Y. Ebihara⁵, T. Motoba⁶, B. Gustavsson⁷, U. Brändström⁸, Y. Sato⁹, S. Oyama^{10,11}, T. Raita¹², F. Sigernes¹³, S. Nozawa¹⁰, K. Shiokawa¹⁰, M. Kosch^{14,15}, K. Kauristie¹⁶, C. Hall⁷, S. Suzuki¹⁷, Y. Miyoshi¹⁰, A. Gerrard¹⁸, H. Miyaoka¹, and R. Fujii¹⁹

- ¹ National Institute of Polar Research, Japan
- ² The Graduate University for Advanced Studies (SOKENDAI), Japan
- ³ Joint Support-Center for Data Science Research, Research Organization of Information and Systems, Japan
- ⁴ Graduate School of Informatics and Engineering, The University of Electro-Communications, Japan.
- ⁵ Research Institute for Sustainable Humanosphere, Kyoto University, Japan.
- ⁶ The Johns Hopkins University Applied Physics Laboratory, USA.
- ⁷ UiT The Arctic University of Norway, Norway
- ⁸ Swedish Institute of Space Physics, Sweden
- ⁹ Nippon institute of technology, Tokyo, Japan
- ¹⁰ Institute for Space–Earth Environmental Research, Nagoya University, Japan.
- ¹¹ University of Oulu, Finland
- ¹² Sodankylä Geophysical Observatory, Finland
- ¹³ University Centre in Svalbard, Norway
- ¹⁴ South African National Space Agency, South Africa
- ¹⁵ Lancaster University, UK
- ¹⁶ Finnish Meteorological Institute, Finland
- ¹⁷ Aichi University, Japan
- ¹⁸ Center for Solar-Terrestrial Research, New Jersey Institute of Technology, USA.
- ¹⁹ Research Organization of Information and Systems, Japan

Corresponding author: Yasunobu Ogawa (yogawa@nipr.ac.jp)

Abstract (less than 200 words)

This paper introduces a new system that can monitor auroras and atmospheric airglows using a low-cost Watec monochromatic imager (WMI) equipped with a sensitive camera, a filter with high transmittance, and the optics which do not make parallel ray paths. The WMI system with 486-nm, 558-nm, and 630-nm band-pass filters has observable luminosity of about ~200 – 4000 Rayleigh for 1.07-sec exposure time and about ~40 – 1200 Rayleigh for 4.27-sec exposure time, for example. It is demonstrated that the WMI system is capable of detecting 428-nm auroral intensities properly, through comparison with those measured with a collocated electron-multiplying charge-coupled device (EMCCD) imager system with narrower band-pass filter. The WMI system has two distinct advantages over the existing system: One makes it possible to reduce overall costs, and the other is that it enables the continuous observation even under twilight and moonlight conditions. Since 2013 a set of multi-wavelength WMIs has been operating in northern Scandinavia, Svalbard, and Antarctica to study meso- and large-scale aurora and airglow phenomena. Future development of the low-cost WMI system is expected to provide a great opportunity for constructing a global network for multi-wavelength aurora and airglow monitoring.

46

47 Keywords: aurora, airglow, imager, polar ionosphere

48

49

50 **1. Introduction**

51

52 Due to the rapid development of cameras and computers in recent years, various progress and new directions are
53 seen in aurora and airglow observations. For example, electron-multiplying charge-coupled device (EMCCD)
54 cameras and/or Scientific CMOS (sCMOS) cameras are used for ultra-sensitive high-speed aurora observations
55 [e.g., Kataoka et al., 2011; Ozaki et al., 2018], and panchromatic observations (time resolution of about 4-sec)
56 by the all-sky panchromatic camera network have been carried out by the THEMIS Ground Based Observatory
57 (GBO) [e.g., Donovan et al., 2006]. However, it is difficult to discuss the average energy and flux of
58 precipitating electrons quantitatively from observations with the all-sky panchromatic camera network. Also, it
59 is still difficult to develop an observation network using high-specification cameras or monochrome optical
60 systems due to their high costs. Optical instruments with filter wheels have been used for observations of
61 multiple wavelengths. They require mechanical motion, and the temporal resolution of each wavelength is
62 limited to several seconds or longer.

63

64 In this paper, we introduce an observation system which solves some of the problems mentioned above. The
65 observation system, named Watec Monochromatic Imager (WMI), consists of a highly-sensitive camera made
66 by Watec Co. Ltd, a fast lens by Fujinon Co. Ltd, a band-pass filter with high transmittance, and is characterized
67 by an optical system that does not produce parallel light. Cost of the WMI system is about one-hundredth of
68 monochrome EMCCD/sCMOS imager systems, but the system has enough sensitivity for the study of
69 aurora/airglow. The low-cost system therefore enables us to make multi-wavelength and multipoint
70 aurora/airglow observations. We have extended observations of the multi-wavelength WMI imagers in northern
71 Scandinavia, Svalbard, and Antarctica since 2013.

72

73 The WMI system composes of simple and high-transmittance optics with a fisheye lens and an optical filter with
74 high transmittance. The system allows us to obtain images with the time resolution of about 1 sec, and therefore
75 auroral substorms [e.g., Akasofu, 1964] with high spatiotemporal variations and pulsating aurora with a period
76 of about several seconds can be targets to study with the WMI system. Other advances of the WMI system are
77 that (1) maintenance of the WMI system (e.g., replacement of cameras, lenses and filters) is easy, and (2) the
78 WMI system enables the continuous observation even under twilight and moonlight conditions because the risk
79 of the WMI camera damage due to twilight or moonlight is relatively low. Disadvantages of this WMI system
80 are that (1) the resolution of the WMI camera data is 8 bits (256 gradations) whereas expensive cameras are
81 usually 16 bits (65,536 gradations), (2) contamination of several aurora and airglow emissions near the typical
82 auroral emissions for WMI (428-nm, 558-nm, and 630-nm) has to be taken into account because the WMI
83 system utilizes band-pass filters with a bandwidth of 10 nm, and (3) the WMI system does not utilize a cooled
84 CCD, and the data from the camera is an analog video signal so that its noise level is relatively high.

85

86 When regular observations are performed with the multi-wavelength WMI system at multiple points, a huge
87 amount of data are accumulated. One image of the system has typically 200 k bytes, and a total amount of their
88 data size is about 8 M bytes per second at the current nine stations. A total of approximately 50 T bytes of disk
89 capacity is required in one year. We have also developed a storage and web server system that integrate and
90 maintain the large amounts of WMI data. In this paper, we explain the outline of the low-cost multi-wavelength

91 WMI observation system and discuss the possibilities and the future development based on data/results obtained
92 using the system.

93

94

95 **2. A multi-wavelength WMI imager system**

96

97 Figure 1 shows examples of multi-wavelength WMI cameras in Tromsø, Norway and Longyearbyen, Svalbard.
98 Eight cameras are installed and operated in each optical dome with a diameter of approximately 1-m. In addition
99 to the WMI all-sky cameras, narrow field of view (FOV) and/or wide FOV camera(s) are included.

100

101 Figure 2 shows an overview of data flows of (a) the WMI observation system in polar regions and (b) the data
102 processing system in the National Institute of Polar Research (NIPR). Analog video signals coming out of the
103 WMI cameras are converted into digital images (with a jpeg format) by a video encoder, and then the images are
104 stored in two PCs in the beginning. The image data are compiled as a tar file every hour and stored in Network
105 Attached Storage (NAS) next. The data are regularly downloaded to NIPR using another PC for data transfer.
106 This data transfer is divided into two types: Transfer of real-time data open to the public (including keogram
107 created automatically at the observation sites) and data transfer of raw images. When transferring raw data, a
108 considerable load on the network occurs, and it causes failure of transferring and storing real-time images. To
109 avoid the problem, we constructed two separated network groups in the WMI system using two routers and NAS
110 with two network ports: (i) A network group for real-time data acquisition from the video encoder to the PCs and
111 (ii) a network group for subsequent data transfer to outside.

112

113 The optical data transferred to NIPR has been stored in multiple NAS, and secondary processing is performed
114 using several workstations. Some of the jpeg image files have been converted to CDF data format files, in
115 collaboration with IUGONET project [e.g., Hayashi et al., 2013; Tanaka et al., 2013]. The IUGONET developed
116 an integrated analysis system in collaboration with the SPEDAS project [Angelopoulos et al., 2018]. Most of the
117 WMI databases are open to the public via a web page (<http://pc115.seg20.nipr.ac.jp/www/opt/index.html>).

118

119 Table 1 shows the individual device names used in the WMI system and their specifications. The WAT-910 HX
120 camera made by Watec Co. has been used for the system since 2013. The camera has four times higher
121 sensitivity than the previous camera (WAT-120 N+ made by Watec Co.) which had been used before 2013. Also,
122 color cameras named WAT-233 and WAT-221S2 have been used to distinguish clouds and auroras. Fujinon's
123 fisheye lens (F1.4) has been used, and also wide/narrow FOV observations are simultaneously used. For the
124 three colors (428-nm, 558-nm, and 630-nm), a band-pass filter having the full width at half maximum (FWHM)
125 of 10 nm is used. In addition, a wider band-pass filter with FWHM of 50 nm for auroras at a wavelength of
126 ~670-nm is also used. The top part of the Watec camera is cut to insert the bandpass filter between the lens and
127 CCD surface of the camera. The video encoders, AXIS Q7404, enables us to transfer a large amount of data
128 from multiple cameras to PCs via Gigabit Ethernet cables.

129

130 **3. Calibration of filters and sensitivities of the WMI system**

131

132 For monochrome aurora/airglow imagers such as ASI-1 and ASI-2 [Taguchi et al., 2004], an optical system with
133 a parallel ray path has been designed. The parallel ray path is created by combining numerous lenses, and
134 consequently its transmittance is reduced (about 50 – 70%, private communication with Dr. Taguchi). Then, a
135 narrow band-pass interference filter (FWHM: 1.5 ~ 3.0 nm) with transmittance of typically about 40 – 50% has

136 been used for the monochrome imagers. On the other hand, this WMI system does not produce parallel ray path
 137 to prevent a decrease in transmittance, and therefore the light passes the filter obliquely (see Figure 1c). The
 138 all-sky image projected on to the image plane has a diameter of 4.5mm which fits within the CCD chip size of
 139 6.0 mm × 7.4 mm. Since the distance between the CCD surface and the eyepiece lens is about 9 mm, the
 140 incident angles of the ray path are mostly within about 18 deg (= tan⁻¹(3/9)). Based on the condition of the
 141 incident angle when inserting a filter between the eyepiece and the CCD surface, we examined the capability of
 142 the aurora emission observations using the WMI system.

143
 144 Figure 3 shows the angular dependence of the transmission characteristics of the three filters used for typical
 145 auroral emissions (428-nm, 558-nm, and 630-nm) measured with the U-3300 spectrophotometer made by
 146 Hitachi High-Tech Science Corporation. As the incident angle increases, the transmission region shifts to the
 147 shorter wavelength, while the shape of the transmittance band does not change significantly. Their transmittance
 148 is still high (80 – 95%). The stable transmittance of the filters to the incident angle is important when we derive
 149 absolute values of auroral emission intensities. When the angle exceeds 20 degrees, auroral emissions are
 150 outside the passband. Thus we confirmed that the imager system should work if the incident angle to the filter is
 151 within ~18 degrees. Regarding the filter for 630-nm aurora/airglow emission, it was found that the aurora
 152 emission of 636.4-nm is also included slightly when the incident angle is small. The shift of the transmission
 153 region λ_θ can be theoretically described using the following equation.

154
 155
$$\lambda_\theta = \lambda_0 (1 - (Ne / N^*)^2 \sin^2 \theta)^{1/2}$$

 156
$$\sim \lambda_0 (1 - \theta^2 / 2 N^{*2}),$$
 (1)

157
 158 where θ is the incident angle, λ_0 is the wavelength when the incident angle θ equals to zero, Ne is the refractive
 159 index of outside media (equal to 1.0), and N^* is the refractive index of the filter (typically ~2.05 for band-pass
 160 filters by Andover Co.). The theoretical shift values of the center wavelengths are marked by blue symbols in the
 161 bottom of each plot in Figure 3. We found that the theoretical shifts are in good agreement with the observed
 162 shifts.

163
 164 The sensitivity of the WMI system has been calibrated against a National Institute of Standards and Technology
 165 (NIST) traceable 1.9-m integration sphere (Labsphere LMS-760) at NIPR. Figure 4a shows a sample image of
 166 the integration sphere taken using the WMI imager with 558-nm band-pass filter and a 1-sec exposure time. It is
 167 found that the sensitivity is almost circularly symmetric. The background count level is already subtracted by
 168 using a dark image. The original image has a high count area on the upper left of the image, which is considered
 169 to be a characteristic of the CCD image sensor (Sony ICX2428ALL, interline system) of the camera. These
 170 calibration data serve as correction factors for sensitivity field flatness. The optics of the WMI system exhibit
 171 moderate vignetting, similar to the ASI-2 (Taguchi et al., 2004). Sensitivity at the horizon (~230 pixels from the
 172 zenith) is about two thirds of the peak sensitivity at the zenith (see Figure 4b). The ratio of sensitivity at a certain
 173 distance from the zenith to that at the zenith was approximated using the following equation.

174
 175
$$\text{Count}(R) / \text{Count}(R=0) = \alpha \times R^2 + 1$$
 (2)

176
 177 where R indicates radial distance (in pixel). α was estimated to be $\sim 6.3 \times 10^{-6}$, using many samples with several
 178 filters and luminosity. The ratio is used to calculate sensitivity field flatness, and one of the results is shown in
 179 Figure 4c.

180

181 Figure 5 shows relationship between count and Rayleigh at the zenith with four wavelengths. Note that
182 background counts were subtracted before calculating the relationship, because an individual difference of the
183 background offset level (~20-70 counts) exists. The background offset causes a narrower dynamic range, so we
184 have to choose setting of gain and exposure time for aurora/airglow observations carefully. The relationships
185 between count and Rayleigh with 486, 558, and 630-nm band-pass filters are very close, and that with 428-nm
186 filter has higher ratio of count to Rayleigh. This difference mainly comes from characteristics of the spectral
187 sensitivity of the CCD image sensor of the WMI system. The sensitivity at 428-nm wavelength is about 0.6
188 times smaller than that at 558-nm wavelength, and the spectral sensitivity has a peak around 600-nm. The
189 relationship between count and Rayleigh is written using the following equations:

$$190 \quad [\text{Count}'] = 255 \times ([\text{Count}] / 255)^{(1/\gamma)} \quad (3)$$

$$191 \quad [\text{Rayleigh}] = a \times [\text{Count}'] + b \quad (4)$$

192
193 where Count' indicates the "corrected count" using the Gamma correction. We have used the Gamma correction
194 to have a better dynamic range in the dark region, and usually use 0.45 as the Gamma (γ) value. The coefficient
195 values of a and b based on the calibration with four Watec camera and four filters are summarized in Table 2.
196 Each error bar in Figure 5 indicates the standard deviation of counts around the zenith. Basically shorter
197 exposure time of the WMI imager gives a wider dynamic range, but average noise level becomes larger than that
198 with longer exposure time. Table 2 summarizes actual noise level and observable luminosity measured with four
199 wavelengths (428-nm, 486-nm, 558-nm, and 630-nm). The average noise levels in Table 2 were derived from the
200 standard deviation of 9×9 pixels around the zenith when the background luminosity was ~600 Rayleigh. We
201 have confirmed that the average noise levels increase due to increase of shot noise when the background
202 luminosity increases. The average noise levels with the 428-nm filter are larger than those with other three filters.
203 Observable luminosity with the 486-nm, 558-nm, and 630-nm filters and a camera setting of the maximum gain
204 (41 dB) was about 40-4000 Rayleigh for 1.07-sec exposure time. When the exposure time is extended to
205 4.27-sec, the noise level is reduced to about one fourth, but the upper limit of the observable range drops to
206 about 1200 R. Note that available shutter speeds are summarized in Table 1. They are suitable for observations
207 of airglows and weak auroras. On the other hand, the observable luminosity with the 428-nm filter becomes
208 wider than the other three filters. For the purpose of studying of bright auroras such as substorm breakup and
209 auroral arcs, settings of the gain should be changed from the maximum to a lower value (25 dB, for example),
210 because intensity of auroras sometimes exceeds the upper limit. As the H_{β} emissions (486-nm) typically have an
211 intensity of 100-150 R [e.g., Fujii et al., 2009], the WMI system is potentially capable of detecting the H_{β}
212 emissions. We have also confirmed that differences of the relationship between count and Rayleigh according to
213 each individual camera are rather small.

214
215
216 For the band-type auroral emissions at the wavelength of ~670-nm, we have used a filter with FWHM of 50 nm.
217 We have also continuously obtained the 670-nm aurora data with the WMI system at several places, to perform
218 quantitative investigation of auroral emissions. Note that the color cameras (WAT-233 and WAT-221S2) to
219 distinguish clouds and auroras have been utilized without any filter.

220

221

222 **4. Comparison of WMI 428-nm aurora emission data with high-sensitive EMCCD camera data**

223

224 Since auroral emission around 428-nm is known as a band emission, a careful quantitative verification is
225 required for the WMI observation with the 428-nm band-pass filters (FWHM of 10-nm). In this study, we

226 investigated whether the WMI system has the estimation capability of the 428 nm auroral emission intensity, by
227 comparing with 428 nm aurora emission data observed simultaneously by the ASI-2 with the narrow band-pass
228 filter.

229

230 Figure 6 shows the comparison between 428-nm aurora emission intensities around the zenith measured with a
231 WMI imager and monochromatic EMCCD imager at Tromsø between 23 and 24 UT on 14 March 2015. Both
232 imagers utilized 428-nm band-pass filters, but FWHM of the filter for the EMCCD imager was about 2 nm.
233 Exposure time of the WMI and EMCCD imagers were 4.27 sec and 2.00 sec, respectively. As shown in Figure 6,
234 both 428-nm auroral intensities were almost identical throughout the 1-h interval, except for relatively brighter
235 auroral intensities around 23:16 UT and 23:18 UT during which the poleward expanding and intensifying aurora
236 was measured after substorm onset. The WMI imager data were saturated around 23:16 UT, while the WMI
237 auroral intensity around 23:18 UT is weaker than the EMCCD one. This result suggests that, the WMI imager is
238 practically impossible to detect 428-nm auroral emission intensities properly during brighter aurorae or the WMI
239 data must be considered with caution for quantitative investigation of the brighter 428-nm auroral variations (>
240 1800 R). Nevertheless, the WMI imager data are very useful because they are in a fairly good agreement with
241 the EMCCD imager data at least for < 1800 R. We can utilize the WMI system for brighter auroras (> 1800 R) if
242 we change settings of the WMI camera (i.e., shorter exposure time and/or lower gain).

243

244 **5. Locations and acquired data of the WMI imagers**

245

246 Figure 7 shows locations of the WMI system with FOV coverages projected to 110 km and 250 km altitudes.
247 Their locations are summarized in Table 3. Distribution of the WMI imagers in northern Scandinavia is rather
248 dense, in the horizontal range of about 50-500 km. The distribution of multipoint sites is suitable for research on
249 three-dimensional structures of auroras using the auroral tomography method [e.g., Aso et al., 1998; Tanaka et
250 al., 2011]. 428-nm and 558-nm monochromatic aurora data obtained at the multipoint sites will be newly used
251 for the mesoscale auroral research, in combination with the current European incoherent scatter (EISCAT) radars
252 and future EISCAT_3D radar system [e.g., McCrea et al., 2015; Tsuda et al., 2017]. Figure 8 shows examples of
253 auroral images taken by the WMI system, and a result of aurora computed tomography analysis by using the
254 WMI auroral images taken at Skibotn, Kilpisjarvi, and Tjautjas at 18:12:21 UT on February 19, 2018. The
255 tomography result shows height variations of the 558-nm auroral arc along geographic longitude (See Figure 8b).
256 Intensity of the auroral arc peaks at an altitude of about 115 km and extends to an altitude of about 140 km. On
257 the other hand, multipoint observations of 630 nm emission in the horizontal range of about a few 1000 km are
258 useful for studies on large scale phenomena such as dynamic variation of auroral oval and drift motion of polar
259 patches. Longyearbyen in Svalbard, South Pole and McMurdo stations are often located in the polar cap region,
260 so their 630 nm emission data have been used for research on the polar patches. The WMI system will be also
261 used for study on geomagnetically conjugate auroras in the auroral zone, polar cap, and sub-auroral regions.

262

263 Table 4 summarizes the status of WMI observations at each site. We started monochromatic imager observations
264 in Tromsø and Longyearbyen in 2013, and have been extended the observations in northern Scandinavia and
265 Antarctica. The camera data have been complementarily used with a collocated high sensitivity EMCCD all-sky
266 camera system at each site. Typical exposure time we used is 4-sec for 428-nm emission, 1-sec for 558-nm
267 emission, and 4-sec for 630-nm emission. They are faster than those of the all-sky imager (ASI) that has been
268 operated at the South Pole Station [Ebihara et al., 2007], for example. The 630-nm emission data are used not
269 only for auroral study, but also airglow observation such as polar patches in the polar cap region. Panchromatic
270 and color all-sky camera observations have been also continuously conducted for dayside auroral pulsation study

271 [e.g., Motoba et al., 2017] even during new moon periods, as well as narrow/wide FOV camera observations
272 mentioned in the previous section. At the South Pole and McMurdo stations, all the cameras can be operated for
273 24 hours a day between April and August.

274

275 In the future, similar WMI systems will be installed in Sanae (South Africa), Maitri (India), and Princess
276 Elisabeth (Belgium) stations in Antarctica under international collaborations. The installation realizes a wide
277 area coverage of auroral/airglow observations and is expected to contribute to the quantitative understanding of
278 aurora physics including interhemispheric auroral research [e.g., Motoba et al., 2012]. Most of the data obtained
279 by the multipoint observations with the WMI system will be converted into CDF format files under the
280 IUGONET project, and they can be handled in a unified manner with software packages provided by the
281 SPEDAS project.

282

283

284 **5. Summary**

285

286 This paper has indicated that the WMI observation – which utilizes an inexpensive imager system equipped with
287 a sensitive Watec camera, a filter with high transmittance, and the optics which does not make a parallel ray path
288 – is effective for research on auroras and atmospheric airglows. Cost of the WMI system is roughly two orders
289 lower than those of monochrome imagers conventionally used for aurora/airglow studies. Compared to
290 conventional imager systems, installation of the WMI system in multiple places is easier, and the risk of the
291 WMI camera damage due to twilight or moonlight is relatively low. It is therefore expected that an increase of
292 the number of the WMI cameras realizes observations with various settings according to the required
293 wavelength and necessary observable luminosity range, and wide-area coverage by multipoint observations. In
294 particular, it is important to obtain (1) 428-nm auroral data at multipoint sites (located in the horizontal range of
295 about 50-100 km) for research on three-dimensional structure of auroras using the auroral tomography method,
296 and (2) multipoint observations with a wavelength of 630-nm (in the horizontal range of about a few 1000 km)
297 for study of large scale phenomena such as dynamic variation of the auroral oval and drift motion of polar
298 patches. It is also expected that the system will be effectively utilized for the study of airglow in mid- and low
299 latitude ionosphere (for examples, observations of the atmospheric gravity wave and plasma bubble in the
300 equatorial region). Thus the WMI system is expected to be further developed and spread to the global-scale
301 upper atmospheric observations of multi-wavelength auroras and airglows. Most of the current WMI databases
302 are open to the public via the web page (<http://pc115.seg20.nipr.ac.jp/www/opt/index.html>).

303

304

305

306

307 **Acknowledgments:**

308

309 We thank I. Sugita and Y. Kadowaki of the National Institute of Polar Research (NIPR), for their helpful support
310 of the MWI data management and calibration. This research was financially supported by the Grants-in-Aid for
311 Scientific Research S (15H05747), Scientific Research B (17H02968) and Scientific Research C (17K05672) by
312 the Ministry of Education, Science, Sports and Culture, Japan. This work was also supported by
313 ROIS-DS-JOINT (001RP2018, and 019RP2018). The WMI system was calibrated at the calibration facility of
314 NIPR, Japan. The production of this paper was supported by a NIPR publication subsidy. This work was
315 partially carried out at the joint research workshop of the Institute for Space-Earth Environmental Research
316 (ISEE), Nagoya University.

317

318 **References:**

319

320 Akasofu S-I., The development of the auroral substorm. *Planet. Space Sci.*, Vol. 12 (1964), pp 273-282.

321 Angelopoulos, V., P. Cruce, A. Drozdov, E. W. Grimes, N. Hatzigeorgiu, D. A. King, D. Larson, J. W. Lewis, J.
322 M. McTiernan, D. A. Roberts, C. L. Russell, T. Hori, Y. Kasahara, A. Kumamoto, A. Matsuoka, Y. Miyashita,
323 Y. Miyoshi, I. Shinohara, M. Teramoto, J. B. Faden, A. J. Halford, M. McCarthy, R. M. Millan, J. G. Sample,
324 D. M. Smith, L. A. Woodger, A. Masson, A. A. Narock, K. Asamura, T. F. Chang, C.-Y. Chiang, Y. Kazama,
325 K. Keika, S. Matsuda, T. Segawa, K. Seki, M. Shoji, S. W. Y. Tam, N. Umemura, B.-J. Wang, S.-Y. Wang, R.
326 Redmon, J. V. Rodriguez, H. J. Singer, J. Vandegriff, S. Abe, M. Nose, A. Shinbori, Y.-M. Tanaka, S. UeNo,
327 L. Andersson, P. Dunn, C. Fowler, J. S. Halekas, T. Hara, Y. Harada, C. O. Lee, R. Lillis, D. L. Mitchell, M.
328 R. Argall, K. Bromund, J. L. Burch, I. J. Cohen, M. Galloy, B. Giles, A. N. Jaynes, O. Le Contel, M. Oka, T.
329 D. Phan, B. M. Walsh, J. Westlake, F. D. Wilder, S. D. Bale, R. Livu, M. Pulupa, P. Whittlesey, A. DeWolfe, B.
330 Harter, E. Lucas, U. Auster, J. W. Bonnell, C. M. Cully, E. Donovan, R. E. Ergun, H. U. Frey, B. Jackel, A.
331 Keiling, H. Korth, J. P. McFadden, Y. Nishimura, F. Plaschke, P. Robert, D. L. Turner, J. M. Weygand, R. M.
332 Candey, R. C. Johnson, T. Kovalick, M. H. Liu, R. E. McGuire, A. Breneman, K. Kersten, P. Schroeder
333 (2018), The Space Physics Environment Data Analysis System (SPEDAS), *Space Sci. Rev.*, 215:9,
334 <https://doi.org/10.1007/s11214-018-0576-4>.

335 Aso, T., Ejiri, M., Urashima, A., Miyayaka, H., Steen, A., Brandstrom, U., and Gustavsson, B. (1998), First
336 results of auroral tomography from ALIS-Japan multi-station observations in March, 1995, *Earth Planets
337 Space*, 50, 81–86.

338 Donovan, E.F., S. Mende, B. Jackel, H. Frey, M. Syrjäsuo, I. Voronkov, T. Trondsen, L. Peticolas, V.
339 Angelopoulos, S. Harris, M. Greffen, M. Connors (2006), The THEMIS all-sky imaging array—system
340 design and initial results from the prototype imager. *J. Atmos. Terr. Phys.* 68, 1472–1487.

341 Ebihara, Y., Y.-M. Tanaka, S. Takasaki, A. T. Weatherwax, and M. Taguchi (2007), Quasi-stationary auroral
342 patches observed at the South Pole Station, *J. Geophys. Res.*, 112, A01201, doi:10.1029/2006JA012087.

343 Fujii, R., Y. Iwata, S. Oyama, S. Nozawa, and Y. Ogawa (2009), Relations between proton auroras, intense
344 electric field, and ionospheric electron density depletion, *J. Geophys. Res.*, VOL. 114, A09304,
345 doi:10.1029/2009JA014319.

346 Hayashi, H., Y. Koyama, T. Hori, Y. Tanaka, S. Abe, A. Shinbori, M. Kagitani, T. Kouno, D. Yoshida, S. UeNo,
347 N. Kaneda, M. Yoneda, N. Umemura, H. Tadokoro, T. Motoba and IUGONET project team (2013),
348 Inter-university Upper Atmosphere Global Observation NETwork (IUGONET), *Data Sci. J.*, 12,
349 WDS179-WDS184, doi: 10.2481/dsj.WDS-030.

350 Kataoka, R., Y. Miyoshi, T. Sakanoi, A. Yaegashi, Y. Ebihara, and K. Shiokawa (2011), Ground-based

351 multispectral high-speed imaging of flickering aurora, *Geophys. Res. Lett.*, Vol. 38 (14).
352 McCrea, I. W., A. Aikio, L. Alfonsi, E. Belova, S. Buchert, M. Clilverd, N. Engler, B. Gustavsson, C.
353 Heinselman, J. Kero, M. Kosch, H. Lamy, T. Leyser, Y. Ogawa, K. Oksavik, A. Pellinen-Wannberg, F. Pitout,
354 M. Rapp, I. Stanislawski, and J. Vierminen (2015), The science case for the EISCAT_3D radar, *Progress in*
355 *Earth and Planetary Science*, doi:10.1186/s40645-015-0051-8.
356 Motoba, T., K. Hosokawa, A. Kadokura, and N. Sato, Magnetic conjugacy of northern and southern auroral
357 beads, *Geophys. Res. Lett.*, Vol. 39 (2012), L08108, doi:10.1029/2012GL051599.
358 Motoba, T., Ebihara, Y., Kadokura, A., Engebretson, M. J., Lessard, M. R., Weatherwax, A. T., and Gerrard, A. J.
359 (2017), Fast- moving diffuse auroral patches: A new aspect of daytime Pc3 auroral pulsations, *J. Geophys.*
360 *Res. Space Physics*, 122, 1542– 1554, doi:10.1002/2016JA023285.
361 Ogawa, Y., A. Kadokura, T. Motoba, Y. Tanaka, and K. Hosokawa (2013), Processing and visualization of large
362 amounts of auroral data obtained with All-sky/Narrow field-of-view parallel imagers in Tromso and
363 Longyearbyen, *Journal of Space Science Informatics Japan*, vol. 2, 51-61.
364 Ozaki, M., K. Shiokawa, Y. Miyoshi, K. Hosokawa, S. Oyama, S. Yagitani, Y. Kasahara, H. Kojima, Y. Kasaba,
365 S. Matsuda, R. Kataoka, Y. Ebihara, Y. Ogawa, Y. Otsuka, S. Kurita, R. Moore, Y. Tanaka, M. Nose, T.
366 Nagatsuma, M. Connors, N. Nishitani, Y. Katoh, M. Hikishima, A. Kumamoto, F. Tsuchiya, A. Kadokura, T.
367 Nishiyama, T. Inoue, K. Imamura, A. Matsuoka, and I. Shinohara (2018), Microscopic observations of
368 pulsating aurora associated with chorus element structures: Coordinated Arase satellite: PWING observations,
369 *Geophys. Res. Lett.*, DOI: 10.1029/2018GL079812.
370 Taguchi, M., M. Ejiri, and K. Tomimatsu (2004), A new all-sky optics for aurora and airglow imaging, *Adv.*
371 *Polar Upper Atmos. Res.*, 18, 140–148.
372 Tanaka, Y.-M., T. Aso, B. Gustavsson, K. Tanabe, Y. Ogawa, A. Kadokura, H. Miyaoka, T. Sergienko, U.
373 Brändström, and I. Sandahl (2011), Feasibility study on Generalized - Aurora Computed Tomography, *Ann.*
374 *Geophys.*, vol. 29, 551-562.
375 Tanaka, Y., A. Shinbori, T. Hori, Y. Koyama, S. Abe, N. Umemura, Y. Sato, M. Yagi, S. UeNo, Satoru, A. Yatagai,
376 Y. Ogawa, and Y. Miyoshi (2013), Analysis software for upper atmospheric data developed by the IUGONET
377 project and its application to polar science, *Advances in Polar Science*, doi: 10.3724/SP.J.1085.2013.00231,
378 vol. 24, No. 4, 231-240.
379 Tsuda, T., M. Yamamoto, H. Hashiguchi, K. Shiokawa, Y. Ogawa, S. Nozawa, H. Miyaoka and A. Yoshikawa
380 (2016), A proposal on the study of solar-terrestrial coupling processes with atmospheric radars and
381 ground-based observation network, *Radio Science*, 51, doi: 10.1002/2016RS006035.
382
383

384

385 **Figure captions:**

386

387 Figure 1: Pictures of the WMI imagers in (a) Tromsø and (b) Longyearbyen. The system includes several all-sky
388 cameras with filters of different wavelengths, and also narrow field of view (FOV) and/or wide FOV camera(s).
389 (c) Schematic illustration of the WMI imager with the Fujinon's fish-eye lens, Watec camera, and the Techspec's
390 band-pass filter.

391

392 Figure 2: An overview of the WMI system. It consists of (a) the imager system at observation sites and (b) the
393 data servers in the National Institute of polar research (NIPR). Arrows in the figure indicate flows of image data.

394

395 Figure 3: Transmittances of three filters with wavelengths of (a) 428-nm, (b) 558-nm, and (c) 630-nm. Each line
396 indicates different incident angles between 0 and 20 degrees. Three vertical lines indicate the locations of auroral
397 emissions at wavelengths of 427.8-nm, 557.7-nm, and 630.0-nm. The symbols marked in the bottom of each plot
398 indicate theoretical changes of the center wavelength of each filter based on equation 1.

399

400 Figure 4: Examples of (a) an original image, (b) the limb darkening characteristics of the WMI imager, and (c) a
401 calibrated image after flat field correction. Background noise level was subtracted before the flat field correction.
402 Note that all the WMI cameras use the settings of a gamma value of 0.45 and the maximum gain value (41 dB).

403

404 Figure 5: The relationship between the corrected count and Rayleigh for the WMI system with four different
405 wavelengths (428, 486, 558, and 630-nm) and different exposure times (1.07-sec and 4.27-sec). Note that all the
406 WMI cameras use the settings of a gamma value of 0.45 and the maximum gain value (41 dB).

407

408 Figure 6: Comparison of 428-nm emission data between the WMI system (red) and the ASI-2 with EMCCD
409 imager (black), obtained in Tromsø on March 14, 2015. A dashed line indicates the upper limit of WMI
410 observation with the settings of 4.27-sec exposure time, a gamma value of 0.45, and the maximum gain value
411 (41 dB).

412

413 Figure 7: Locations of the WMI system, and coverages of observable regions projected into (green) 110 km and
414 (red) 250 km altitudes. The edge of the all-sky circle is at 70 degrees from the zenith.

415

416 Figure 8: (Left) Auroral images at a wavelength of 558 nm observed with WMI at 6 locations at 18:12:21 UT on
417 February 19, 2018. Each image is projected into 110 km altitude. (Right) A result of aurora computed
418 tomography analysis by using the WMI auroral images taken at Skibotn, Kilpisjarvi, and Tjautjas at 18:12:21
419 UT on February 19, 2018. The center position of panels a, b, and c is set at 68.58 deg geographic north and
420 20.63 deg geographic east, and x and y indicate the local Cartesian coordinates in the zonal and meridional
421 directions.

422

423

424

425

426 Table 1: Product names and their specifications composing the WMI system

427

Camera	<p>Water WAT-910HX/RC (CCD: Sony ICX428ALL, CCD size: 7.40 mm × 5.95 mm (1/2 inch)) Minimum Illumination 0.0000025 Lux (× 256 frames, F1.4) Shutter speeds used: 0.25, 0.53, 1.07, 2.14, and 4.27 sec (×256 frames)</p>
Lens	<p>Fujinon Fish-eye lens YV2.2x1.4A-SA2 Focus length: 1.4-3.1 mm, F1.4, FOV: 185° × 185°</p>
Optical filter	<p>Techspec, 25 mm diameter, hard coated OD4 10 nm band-pass filter Center wavelengths: 430, 488, 560, and 632 nm FWHM: 10 nm</p> <p>Techspec, 25 mm diameter, hard coated OD4 50 nm band-pass filter Center wavelength: 675 nm FWHM: 50 nm</p>
Video encoder	<p>AXIS Q7404 Image resolution: 640 pixels × 480 pixels, Image format: jpeg (8bit), AXIS Q7424-R Image resolution: 640 pixels × 480 pixels, Image format: jpeg (8bit)</p>

428

429

430

431 Table 2: Summary of average noise level and observable luminosity at each wavelength. The observable
432 luminosity was estimated taking subtraction of background (~20-80 counts) and the maximum count (256 counts,
433 8-bit) into account. All the WMI cameras use the settings of a gamma correction value of 0.45 and the maximum
434 gain value (41 dB). The average noise levels were calculated when the background luminosity was ~600
435 Rayleigh. The a and b in the table indicate each coefficient of Equation 4.

436

Aurora/air glow emission	Wavelength of filter	Exposure time	Serial number of camera	a	b	Average noise level	Observable luminosity
428 nm (N ₂ ⁺)	430±5 nm	1.07 sec	03632	45.01	99.15	190 R	220-6000 R
		4.27 sec	03632	10.25	30.03	60 R	70-1800 R
486 nm (H _β)	488±5 nm	1.07 sec	03633	20.95	112.83	180 R	230-4000 R
		4.27 sec	03633	5.27	16.68	40 R	40-1200 R
558 nm (OI)	560±5 nm	1.07 sec	03631	21.63	118.85	200 R	200-4000 R
		4.27 sec	03631	5.54	40.95	60 R	90-1200 R
630 nm (OI)	632±5 nm	1.07 sec	02933	22.69	90.92	140 R	200-4000 R
		4.27 sec	02933	5.52	8.92	30 R	20-1200 R

437

438

439

Table 3: Locations of multi-wavelength WMI observation stations, including possible ones near future (in Italic).

440

Location name	Code	Geographic Latitude (deg)	Geographic longitude (deg)	Geomagnetic latitude (deg)
Longyearbyen	LYR	78.15	16.03	75.16
Tromsø	TRO	69.58	19.22	66.53
Skibotn	SKB	69.35	20.36	66.23
Kilpisjarvi	KIL	69.05	20.78	65.90
Kiruna	KRN	67.84	20.41	64.68
Tjautjas	TJA	67.33	20.75	64.14
Sodankylä	SOD	67.42	26.39	63.96
South pole	SPA	-90.00	139.27	-74.11
McMurdo	MCM	-77.82	166.66	-79.97
<i>Sanae</i>	<i>SAN</i>	<i>-72.67</i>	<i>-2.83</i>	<i>-62.08</i>
<i>Maitri</i>	<i>MAI</i>	<i>-70.77</i>	<i>11.73</i>	<i>-62.83</i>
<i>Princess Elisabeth</i>	<i>PEA</i>	<i>-71.95</i>	<i>23.33</i>	<i>-65.29</i>
<i>Syowa</i>	<i>SYO</i>	<i>-69.19</i>	<i>41.05</i>	<i>-66.69</i>

441

442

443

444 Table 4: Wavelength and exposure time used for the WMI system at each station. Each number in the table
 445 indicates exposure time of WMI camera data (equivalent to its time resolution). Note that asterisk (*) indicates
 446 usage of band-pass filters with wider bandwidth (FWHM of ~100 nm, see Ogawa et al., 2013). “BW” indicates
 447 panchromatic black-white image data, and “Color” indicates color image data taken with WAT-233 (with 4-sec
 448 exposure time) and WAT-221S2 (with 1-sec exposure time).

449

Site	Start	End	428nm	558nm	630nm	670nm	BW	Color
TRO	2011-01	2013-03	1*	1*	1*	-	1	-
	2013-10	2014-03	-	1	4	1	0.5	-
	2014-09	2016-03	4	1	4	1	0.25	4
	2016-09	2019-03	-	1	4	0.5	-	1
LYR	2011-01	2013-03	1*	1*	1*	-	1	-
	2013-10	2014-03	-	1	4	0.5	0.5	-
	2014-09	2016-03	4	1	4	0.5	0.25	4
	2016-09	2019-03	4	1	4	0.5	0.25	1
SPA	2014-04	2014-08	-	0.5	4	-	0.5	-
	2015-03	2015-08	4	1	4	1	0.5	4
	2016-03	2018-08	-	1	4	1	0.5	-
MCM	2015-03	2018-08	-	4	4	1	-	4
KIL	2016-10	2017-03	4	-	-	-	-	-
	2017-03	2017-04	4	1	-	0.5	-	-
	2017-10	2018-03	4	1	-	0.5	-	1
	2018-10	2019-03	2	1	-	0.5	-	1
KRN	2017-01	2019-03	4	1	-	0.5	-	1
TJA	2017-01	2019-03	4	1	-	0.5	-	1
SKB	2018-02	2018-03	2	1	-	-	-	1
	2018-09	2019-03	1	1	1	-	0.5	1
SOD	2016-09	2019-03	-	1	-	-	-	1

450

451

Fig 1

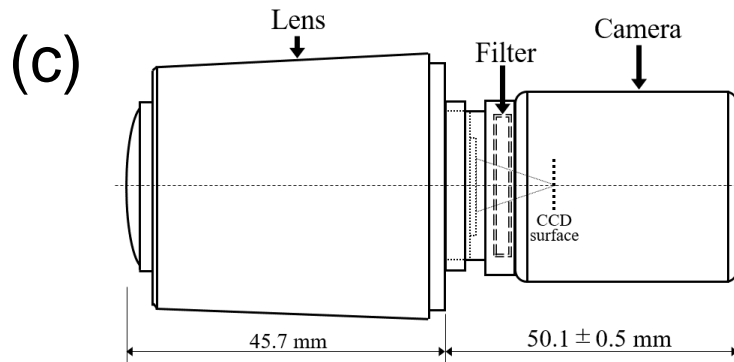


Fig 2

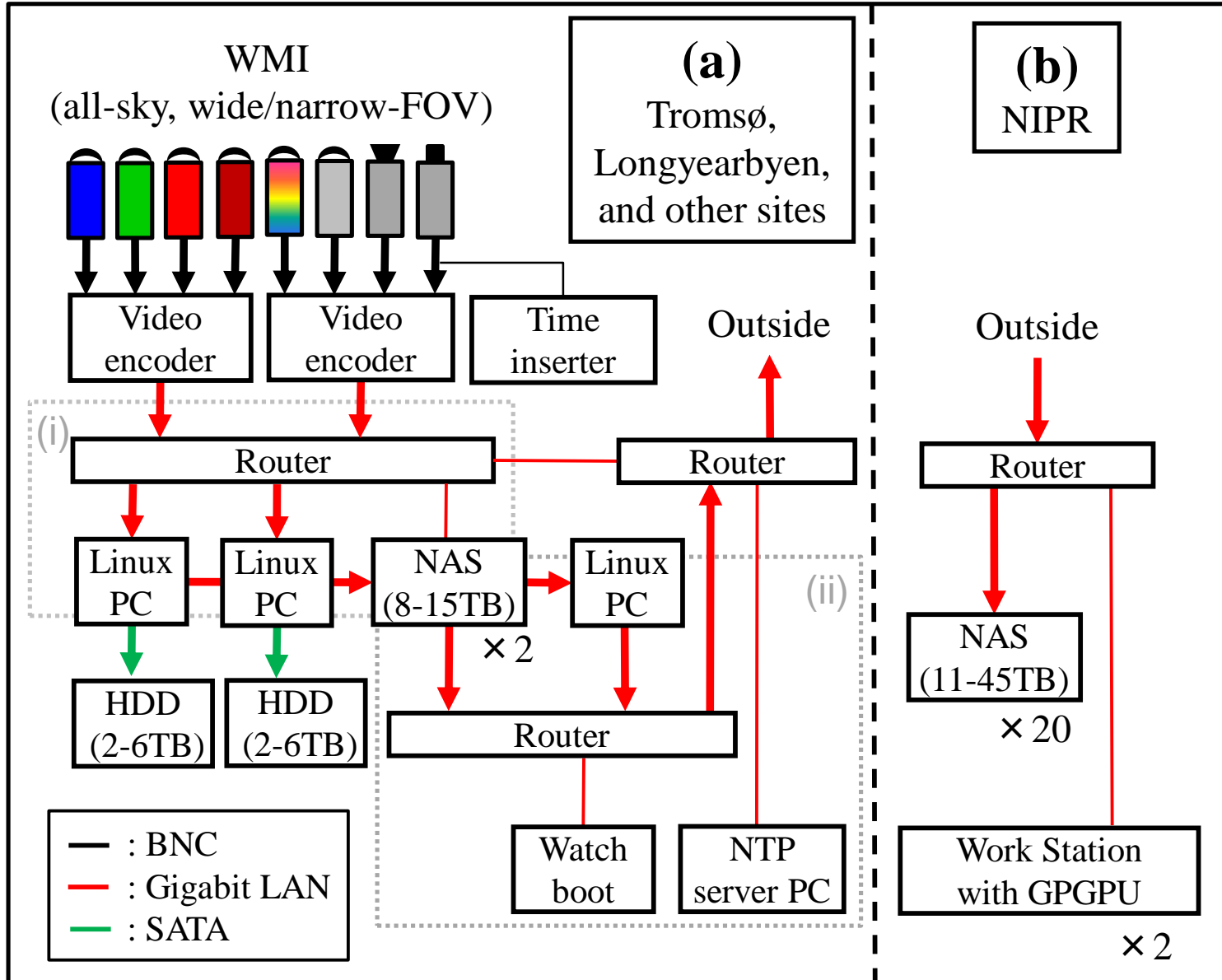
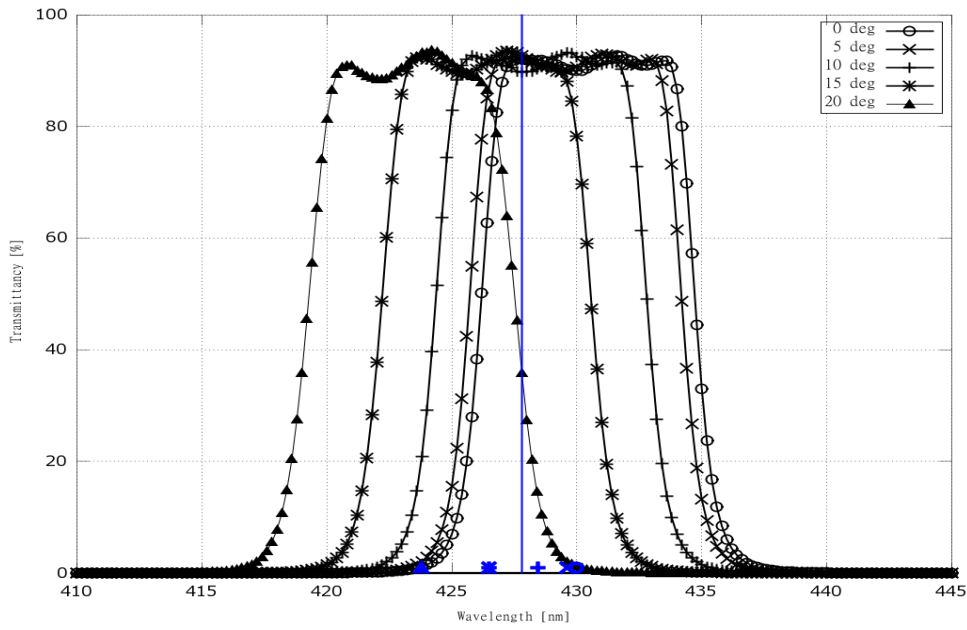
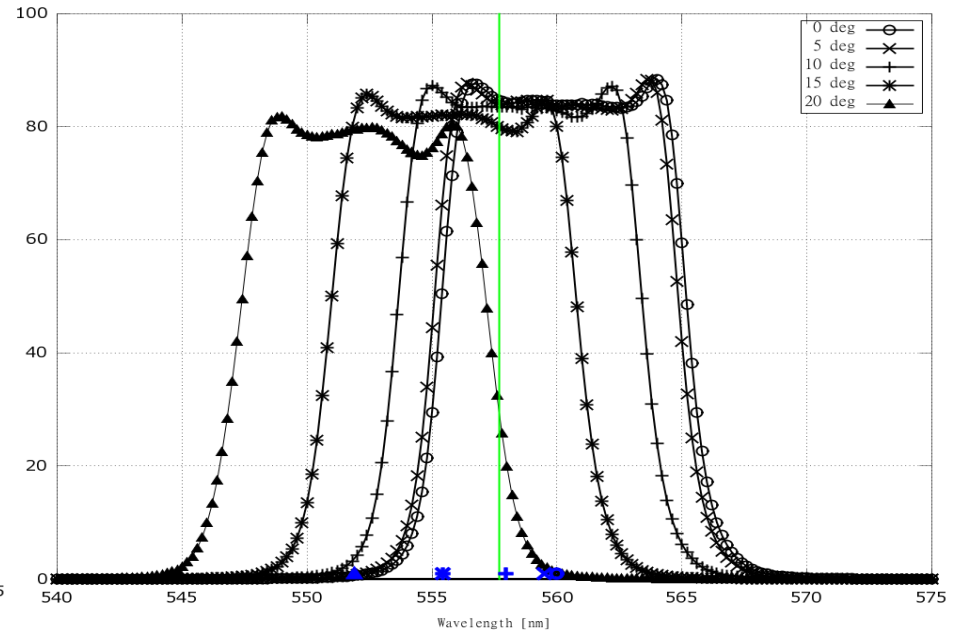


Fig 3

(a) 428 nm



(b) 558 nm



(c) 630 nm

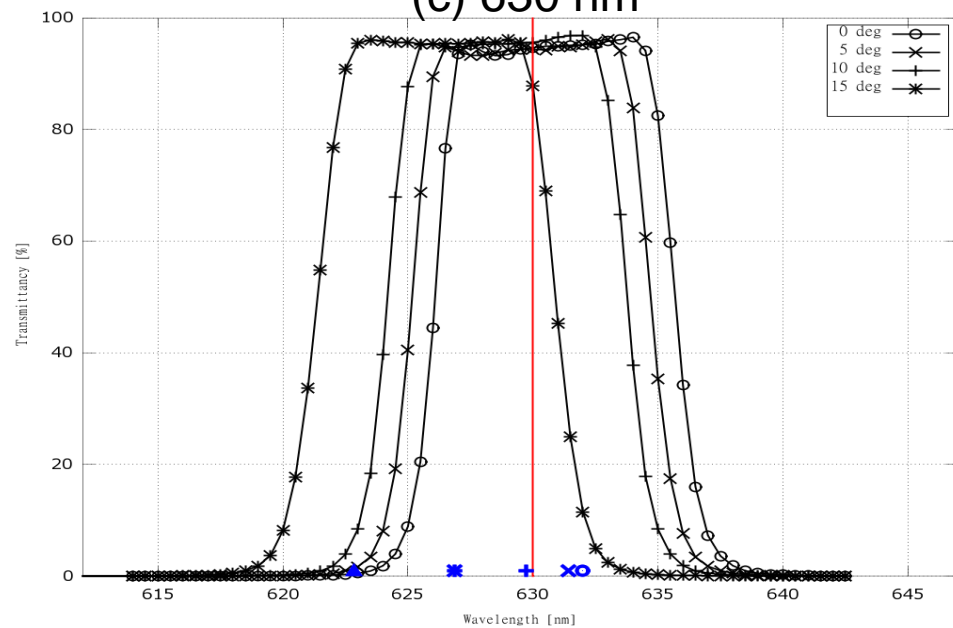
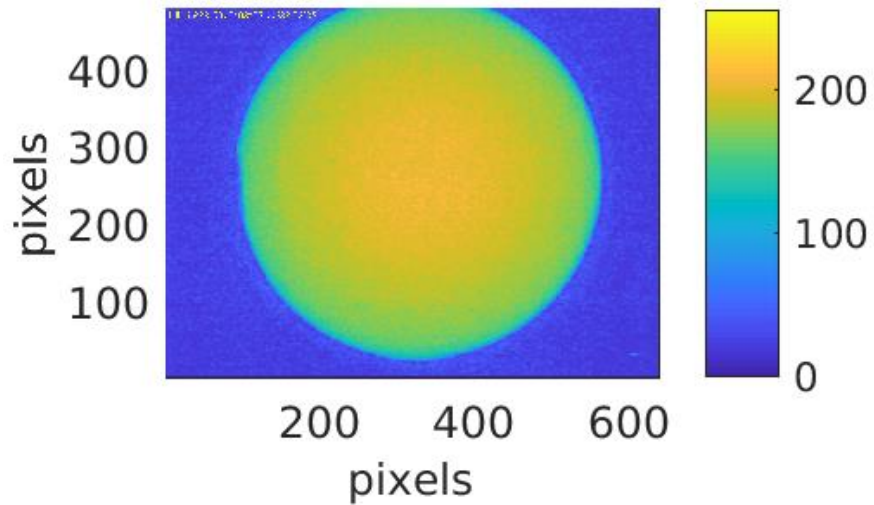
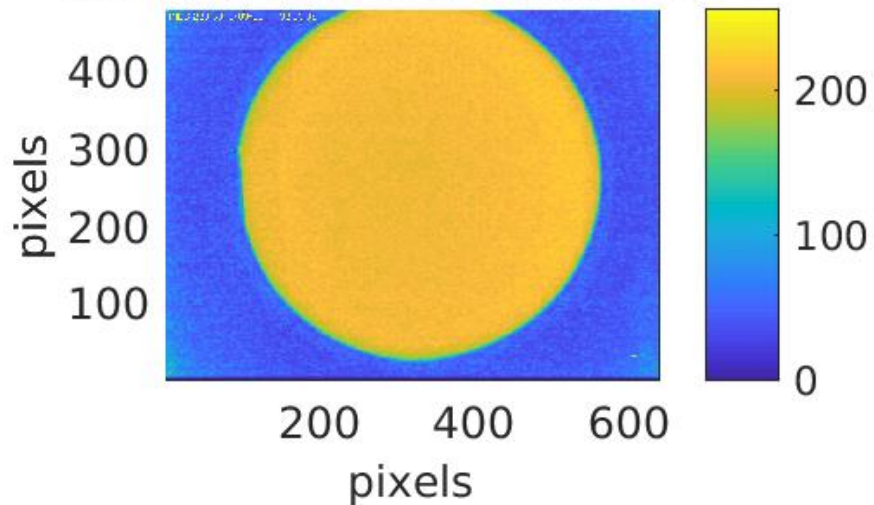


Fig 4

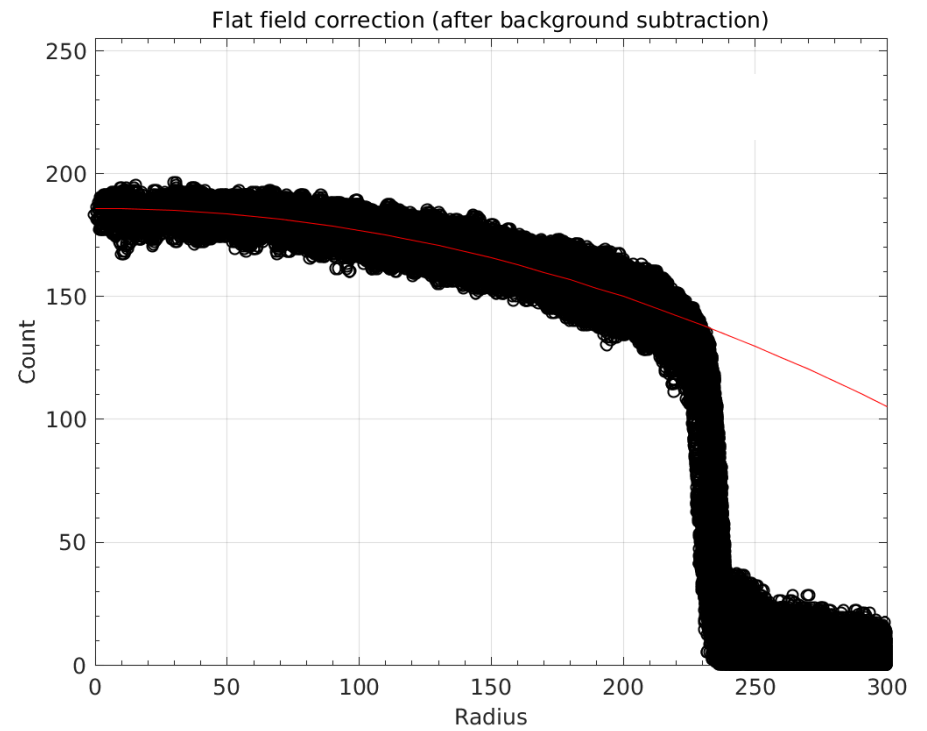
(a) Original image [Count]



(c) After flat field correction [Count]



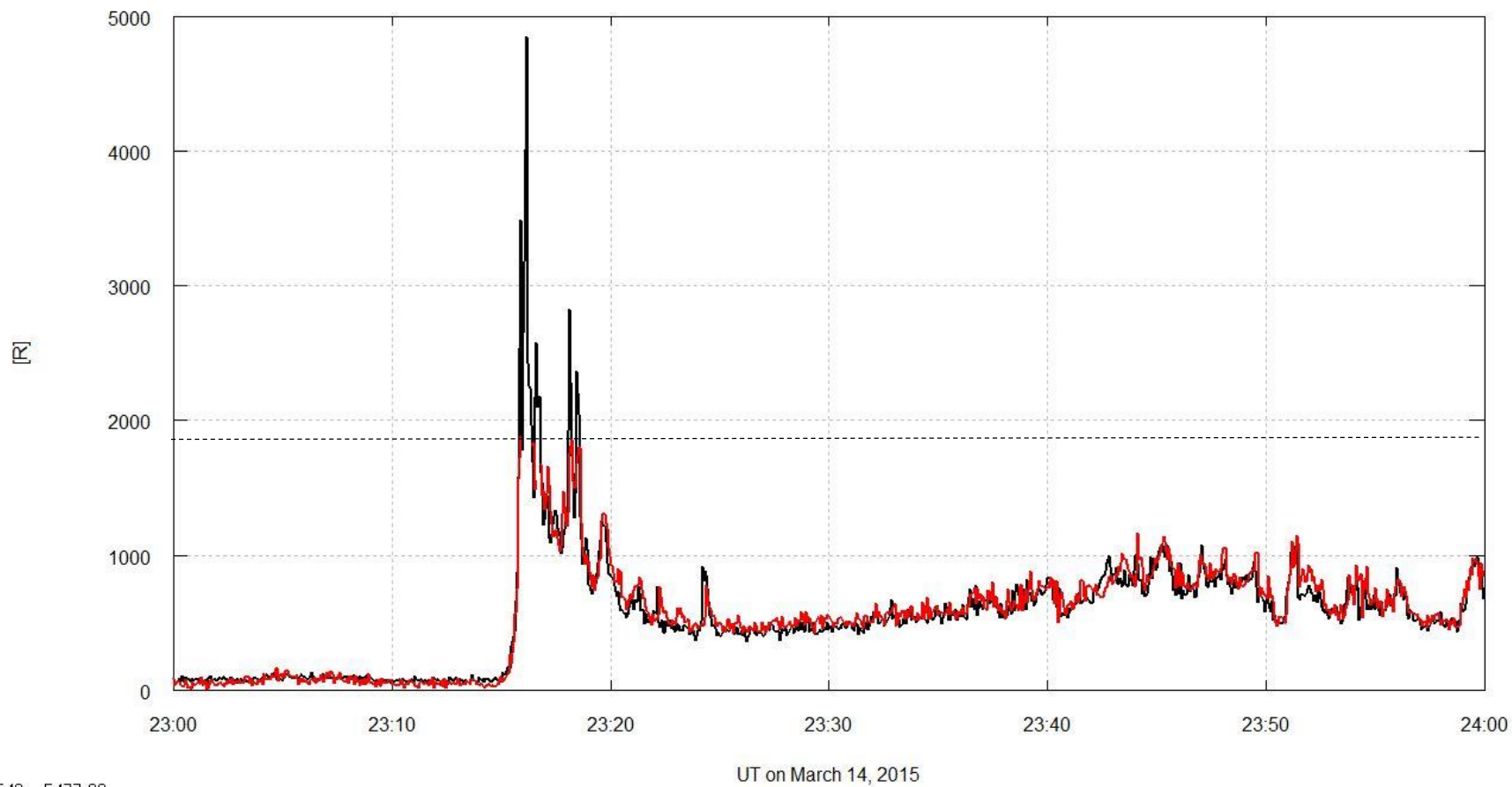
(b)



558nm, 1sec

Fig 6

Water camera, 428nm (Red) and EMCCD imager 428nm (Black), EL: 90 deg



23.4548, 5477.88

Fig 7

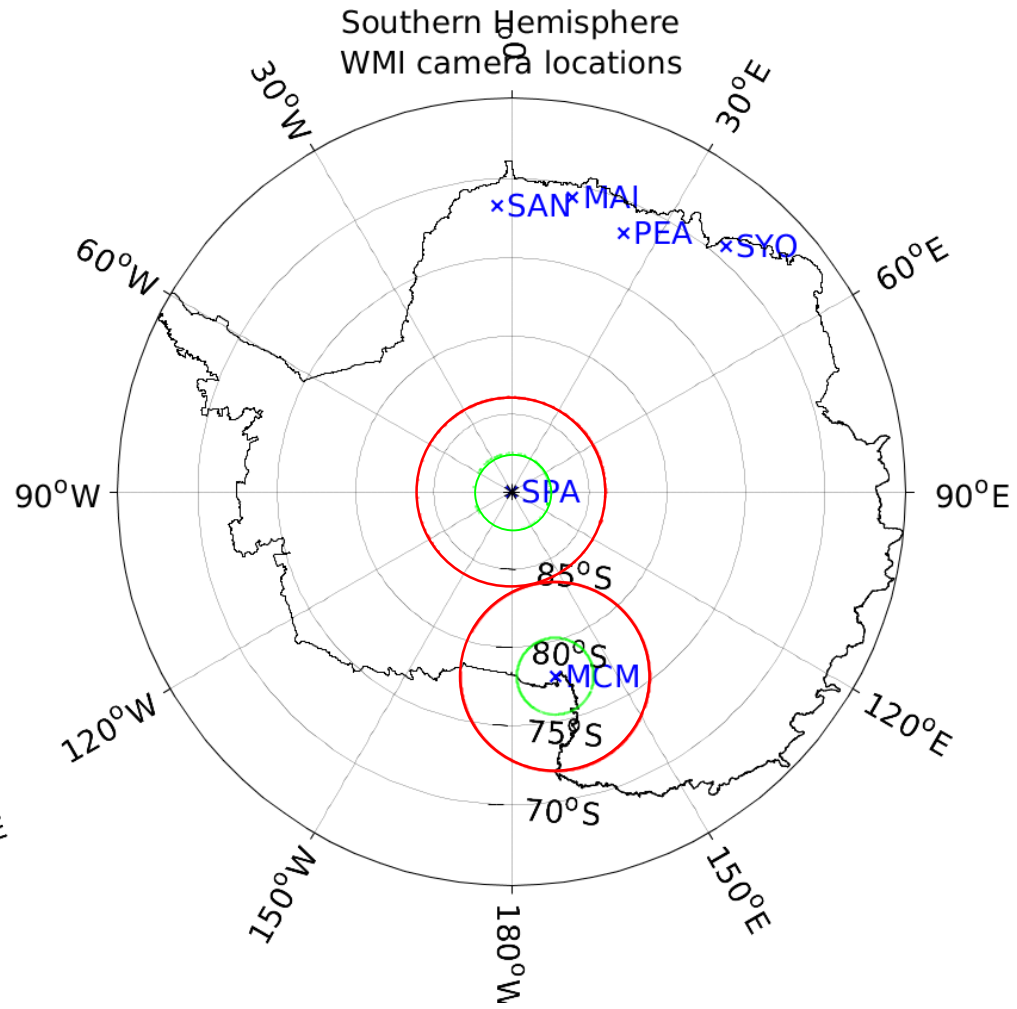
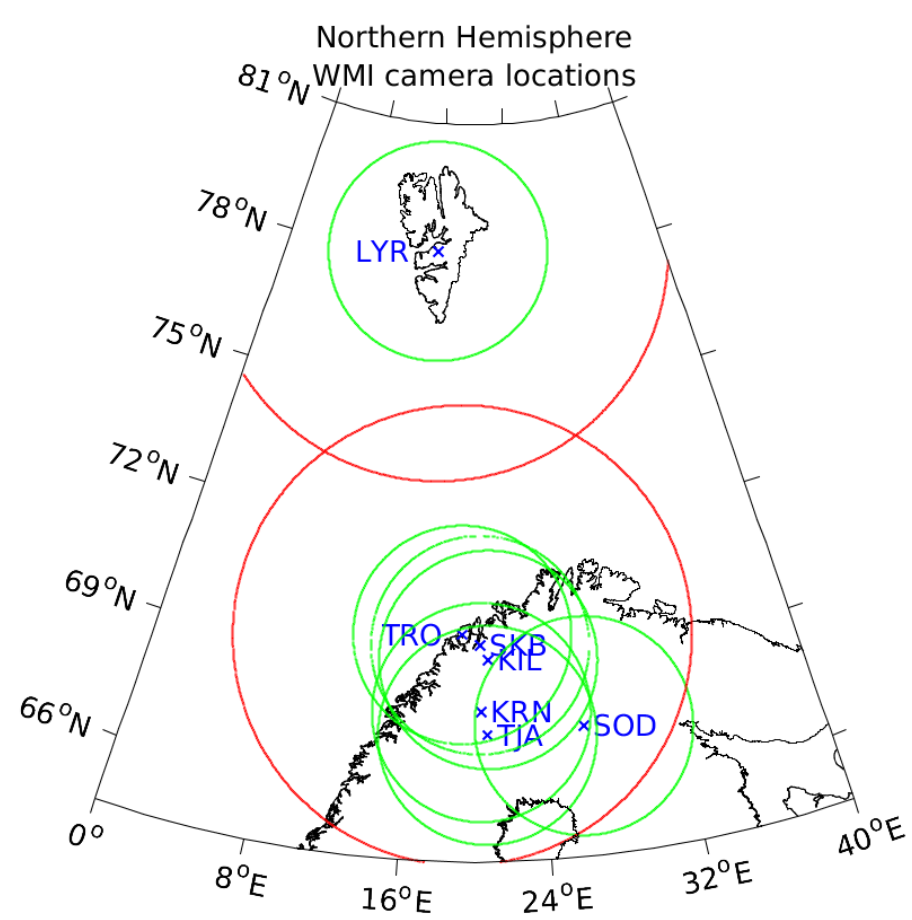


Fig 8

2018-02-19 18:12:21 UT,
558-nm, 1-sec, 110 km altitude

